IEEE Access
Multidisciplinary | Rapid Review | Open Access Journal

IEEE POWER & ENERGY SOCIETY SECTION

Received 12 February 2024, accepted 4 March 2024, date of publication 5 March 2024, date of current version 14 March 2024.

Digital Object Identifier 10.1109/ACCESS.2024.3374214

APPLIED RESEARCH

Simple and Accurate Computation of Rotor Eddy-Current Losses in Surface-Mounted Permanent Magnet Machines Accounting for Magnet Circumferential Segmentation

CESARE CIRIANI, HAMID ALI KHAN, KIROLS MANSOUR, MATTEO OLIVO, AND ALBERTO TESSAROLO, (Senior Member, IEEE)
Engineering and Architecture Department, University of Trieste, 34127 Trieste, Italy
Corresponding author: Alberto Tessarolo (atessarolo@units.it)

ABSTRACT Extensive literature has been produced on the investigation of eddy current losses in Surface-mounted Permanent Magnet (SPM) electric machines in presence of circumferential segmentation by analytical solution of two-dimensional (2D) models. What is missing in the present literature and constitutes the aim of this paper is a simple but accurate procedure enabling the designer to quickly and easily estimate the impact of circumferential segmentation on permanent-magnet loss reduction. The problem is hereinafter addressed in two stages: first the Helmholtz equation is solved in the permanent magnet region neglecting segmentation; then suitable gauge fixing terms are added to the vector potential and eddy current field solutions to account for segmentation. Unlike existing approaches, the method leads to manageable formulas whose accuracy is extensively assessed against finite element simulations on an example SPM machine equipped with a fractional-slot concentrated winding. Furthermore, simple practical rules are derived and validated regarding the impact of magnet segmentation on permanent-magnet losses caused by air-gap magnetic field space harmonics of different orders.

INDEX TERMS Eddy currents, electric machines, losses, permanent magnets, SPM machines.

NOMENCLATURE

p	number of pole pairs;
θ_s	angular coordinate in the stator reference frame;
θ	angular coordinate in the rotor reference frame;
θ_{rot}	rotor position in the stator reference frame;
θ_{rot0}	rotor position at $t = 0$ in the stator reference frame;
R_s	stator bore radius;
R_r	rotor core outer radius;
R_m	permanent magnet outer radius;
L	core axial length;
M	number of permanent magnet segments;
m	magnet segment index ($m = 1, 2 \ldots M$);
r	radial coordinate;
z	axial coordinate;
ω	angular frequency of stator currents;
n	space harmonic order;
κ	harmonic sense of rotation coefficient ($\kappa = \pm 1$);
$\lambda_{n,\kappa}^{real}$	equivalent linear current density function;
$f_{n,\kappa}^{real}$	air-gap magneto-motive force function;
$\Lambda_{n,\kappa}^{max}$	equivalent linear current density magnitude;
$F_{n,\kappa}^{max}$	air-gap magneto-motive force magnitude;
$F_n^{max,FE}$	air-gap magneto-motive force magnitude from FE;
$\omega_{n,\kappa}$	angular frequency of rotor eddy currents;
$\Lambda_{n,\kappa}$	equivalent linear current density phasor;
$F_{n,\kappa}$	air-gap magneto-motive force phasor;
σ	electrical conductivity of permanent magnets;

The associate editor coordinating the review of this manuscript and approving it for publication was Sinisa Djurovic.

μ_0	magnetic permeability of the air;
Z	number of stator slots or teeth;
N_0	number of turns wound around each tooth;
$\mathbf{W}$	winding matrix;
$A^{\text{air}}_{n,\kappa}$	vector potential phasor in the air gap region;
$A^{\text{mag}}_{n,\kappa}$	vector potential phasor in the magnet region;
$B^{\text{air},r}_{n,\kappa}$	radial component of the flux density phasor in the air gap region;
$B^{\text{air},\theta}_{n,\kappa}$	tangential component of the flux density phasor in the air gap region;
$B^{\text{mag},r}_{n,\kappa}$	radial component of the flux density phasor in the magnet region;
$B^{\text{mag},\theta}_{n,\kappa}$	tangential component of the flux density phasor in the magnet region;
$j_{n,\kappa}$	eddy current phasor in permanent magnets;
∇_z	z (axial) component of the gradient operator;
$\phi_{n,\kappa}$	scalar function for defining $j_{n,\kappa}$;
$j^{\text{noseg}}_{n,\kappa}$	eddy current phasor in the permanent magnet region neglecting segmentation;
$j^{\text{seg},m}_{n,\kappa}$	eddy current phasor in the m^{th} magnet segment;
$\phi^m_{n,\kappa}$	scalar function for defining $j^{\text{seg},m}_{n,\kappa}$;
$I^m_{n,\kappa}$	phasor of the total current flowing through the m^{th} magnet segment;
$P^{\text{noseg}}_{n,\kappa}$	eddy current losses in the magnet region neglecting segmentation;
$P^{\text{seg}}_{n,\kappa}$	eddy current losses considering segmentation;
$P^{\text{seg},m}_{n,\kappa}$	eddy current losses in the m^{th} magnet segment;
P_{tot}	total losses in the magnets due to all magneto-motive force space harmonics;
$f_n(M)$	non-dimensional function for permanent magnet loss computation.

I. INTRODUCTION

One of the main issues in the design and operation of SPM machines is the occurrence of eddy-current losses in the permanent magnets [1], [2]. Such losses are potentially dangerous because they cause heating and possible demagnetization risks [3], [4], [5]. A usual countermeasure to mitigate the problem is to subdivide permanent magnets into axial and circumferential segments [6]. Although beneficial for loss reduction, magnet segmentation poses significant challenges when it comes to predict the magnet losses in the design stage. Of course, brute force Finite Element (FE) analysis can be employed [1], [6], [7], [8] leading to very realistic results, but with well-known shortcomings due to the significant computational burden.

As an alternative to FE simulations, the technical literature offers a variety of both 2D and 3D analytical methods to determine eddy-current losses accounting for magnet segmentation.

The 3D analytical approaches are certainly desirable because they can cover both axial and circumferential segmentation. However, there is a price to be paid for tackling the problem through 3D models. For example, in many works the magnet eddy-current reaction field is neglected [9], [10], [11], [12], [13], which is known to possibly cause important errors [14], [15]; in [16] the flux density is supposed to be purely radial, while its tangential component may play a noticeable role in the computation of low-frequency eddy-current losses [15]; the approaches proposed in [15] and [17] are hybrid in the sense that they combine analytical calculations with lengthy 2D or even 3D FE simulations; the method set forth in [18] enjoys the benefit of considering magnetic saturation but requires the numerical solutions of large reluctance network models.

Moving to 2D methods, their obvious limit is that they disregard end effects, i.e. the finite length of magnet segments in the axial direction, and therefore appear little suitable for taking axial segmentation into account. This shortcoming is attenuated by the possibility, which several authors recognize and exploit, to solve the 2D machine model and then consider finite length effects by applying suitable correction coefficients to the results [19], [20]. In some cases, the correction coefficient is directly applied to the 2D model by fictitiously increasing permanent magnet electrical resistivity to account for the resistance of actual 3D eddy current paths [17], [21], [22].

The majority of the 2D analytical methods available in the literature to compute permanent-magnet losses in SPM machines employs the subdomain technique [23], [24], [25], [26], [27], [28], which is mathematically rigorous and exact, but complicated to apply in an application-oriented engineering environment. The method set forth in [20] is more straightforward, but presently applied and validated in the case of a single magnet crossed by a pulsating magnetic field. The procedure described in [21] appears simpler than the subdomain technique but implies the decomposition of the magnetic field wave travelling over a single magnet segment into Fourier series, so that the method may not be straightforward to employ for the designer.

What seems missing in the extensive technical literature available in the field is a practical computation tool which enables the designer to quickly but accurately compute the eddy current losses of an SPM machine with segmented permanent magnets through a well-defined easy-to-implement algorithm. This paper is aimed at providing SPM machine designers with such a tool, considering a 2D machine model and then explicitly addressing only circumferential segmentation. However, as suggested by several authors [17], [19], [20], [21], [22], finite length effects can be, to a first approximation, taken into proper account through correction coefficients, which extends the potential use of the presented procedure to the case of axial segmentation, too.

The methodology used in the paper to obtain easy formulas for the permanent magnet losses as a function of segmentation is the following. Different from what is done in the vast majority of papers dealing with 2D models [15], [21], [23], [24], [25], [26], [27], [28], the magnetic and eddy-current

field equations are not herein solved resorting to Fourier series expansion of the general solution. The alternative idea is, instead, to first solve the Laplace and Helmholtz equations neglecting magnet segmentations, i.e. treating permanent magnets as a continuous cylindrical annulus. The simple solution thus obtained is then corrected considering that the eddy current density expressions are determined up to an additive constant function. Such a gauge is fixed so as to satisfy the constraint that the total current axially flowing through each magnet segment must be zero. In this way, the simple field solution which disregards segmentation is easily adjusted through suitable additive constants to fit the case of an arbitrary number of magnet segments.

For the sake of clarity, the final formulas obtained for permanent magnet eddy-current losses are represented in the form of a flowchart which can be easily implemented in any engineering calculation environment. From the final equations, rules are also derived regarding the effect of segmentation in reducing permanent magnet losses. In particular, it is demonstrated that a condition for the segmentation to be effective in reducing the losses caused by a given air-gap magneto-motive force (MMF) space harmonic of order n is that the number of circumferential segments must be larger than the harmonic order n.

Finally, the proposed algorithm for permanent magnet loss computation is extensively validated against FE simulations on an example SPM machine.

Of course, the analytical approach being presented is advantageous compared to FE simulations because it does not require any model of the machine to be built and solved: once implemented, analytical formulas can be flexibly applied by simply changing input data. Furthermore, they take a fraction of second to solve, while the computation of permanent-magnet losses with FE method typically requires transient (or time stepping) simulations [29] which may take hours to converge to a steady-state condition. On the other hand, FE method is capable of capturing the effects of the machine design details as well as of magnetic saturation, which need to be neglected to obtain manageable analytical formulas [15], [21], [23], [24], [25], [26], [27], [28].

The article is structured as follows. In Section II the model and the problem being tackled are presented along with the assumptions made. In Section III the analytical model solution with the proposed approach is presented. Section IV includes remarks on the practical application of the final formulas derived. Sections V and VI provide a complete assessment of the proposed calculation method by comparison against FE simulations, considering single space harmonics in Section V and then a complete electric machine in Section VI. Finally, Section VII summarizes the main findings and draws the conclusions of the work.

II. PROBLEM AND MODEL DEFINITION

A. MACHINE MODEL DESCRIPTION

With no restriction to generality, we will consider a three-phase SPM machine with p pole pairs, axial length L and with the cross-sectional geometry sketched in Figure 1, where: R_s is the stator bore radius; R_r is the rotor core outer radius; R_m is permanent magnet outer radius; O_s is the stator bore point taken as a reference for polar angles in the stator reference frame; θ_s and r are the polar angle and radius identifying the position of a generic point P placed either in the air gap or in the magnet region.

The rotor is supposed equipped with M magnet segments, sequentially numbered from 1 to M. One side of the first segment is assumed as the reference for identifying the rotor angular position θ_{rot} in the stator reference frame as illustrated in Figure 1. As a consequence, Figure 1 shows that the angular position θ of the generic point P in the rotor reference frame will be such that:

$$\theta_s = \theta_{rot} + \theta \tag{1}$$

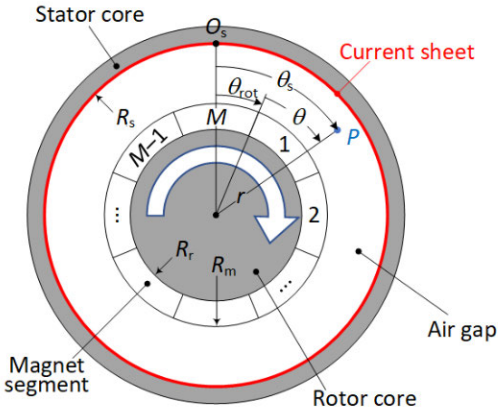

FIGURE 1. Machine model and its polar coordinate system.

The problem being tackled is to determine the eddy currents arising in the permanent magnets when the machine operates at steady state with stator angular frequency $\omega_s = 2\pi f$ (being f the frequency of stator currents) as a consequence of a space harmonic magnetic field of order n, i.e. characterized by n pole pairs. It is worth mentioning that the space harmonic order n is not constrained to be a multiple of the number of pole pairs p (for example let us think of the case of subharmonics in fractional-slot windings machines, wherein $n < p$, [30]). It is well known from the literature that the magnetic field space harmonic of order n can be thought of as produced by a current sheet spread around the stator bore circumference [31] (Figure 1) and characterized by a linear current density:

$$\lambda_{n,\kappa}^{real}(\theta_s, t) = \Lambda_{n,\kappa}^{max} \cos(n\theta_s - \kappa\omega_s t) \tag{2}$$

where $\Lambda_{n,\kappa}^{max}$ is the peak value of the current density and the coefficient κ is equal to either $+1$ or -1 depending on whether the space harmonic field revolves in the same or opposite direction compared to the rotor, respectively. Of course, the expression (1) implies that the origin O_s of the stator-attached coordinate system is placed at the position where the linear current density takes its peak value at $t = 0$.

The linear current density (2) naturally relates to the air-gap MMF $f_{n,\kappa}^{\text{real}}(\theta_s, t)$ so that [31]:

$$\lambda_{n,\kappa}^{\text{real}}(\theta_s, t) = \frac{1}{R_s}\frac{\partial}{\partial\theta_s} f_{n,\kappa}^{\text{real}}(\theta_s, t) \tag{3}$$

In steady-state conditions, the rotor revolves at synchronous speed, hence its angular position can be expressed as:

$$\theta_{\text{rot}} = \frac{\omega_s}{p}t + \theta_{\text{rot0}} \tag{4}$$

where θ_{rot0} is the rotor position at $t = 0$.

By using (1) and (4) in (2), this becomes:

$$\lambda_{n,\kappa}^{\text{real}}(\theta, t) = \Lambda_{n,\kappa}^{\max}\cos\left(n(\theta + \theta_{\text{rot0}}) + \omega_s t\left(\frac{n}{p} - \kappa\right)\right) \tag{5}$$

which represents the stator linear current density expressed in the rotor reference frame. The angular frequency of rotor eddy currents will then be:

$$\omega_{n,\kappa} = \omega_s\left(\frac{n}{p} - \kappa\right) \tag{6}$$

so that (5) can be rewritten as:

$$\lambda_{n,\kappa}^{\text{real}}(\theta, t) = \Lambda_{n,\kappa}^{\max}\cos\left(n(\theta + \theta_{\text{rot0}}) + \omega_{n,\kappa} t\right) \tag{7}$$

In order to separate the dependency on time and space and exploit complex algebra potentials, it is useful to express (7) as:

$$\lambda_{n,\kappa}^{\text{real}}(\theta, t) = \mathcal{R}e\left(\Lambda_{n,\kappa} e^{in\theta} e^{i\omega_{n,\kappa} t}\right) \tag{8}$$

$$\Lambda_{n,\kappa} = \Lambda_{n,\kappa}^{\max} e^{in\theta_{\text{rot0}}} \tag{9}$$

where i is the imaginary unit and $\Lambda_{n,\kappa} e^{in\theta}$ is the space-dependent phasor representing the stator linear current density in the rotor reference frame.

With identical procedure applied to the equivalent MMF we have:

$$f_{n,\kappa}^{\text{real}}(\theta, t) = \mathcal{R}e\left(F_{n,\kappa} e^{in\theta} e^{i\omega_{n,\kappa} t}\right) \tag{10}$$

$$F_{n,\kappa} = F_{n,\kappa}^{\max} e^{in\theta_{\text{rot0}}} \tag{11}$$

and, based on (4) and (1), the following relationship holds:

$$\Lambda_{n,\kappa} e^{in\theta} = \frac{1}{R_s}\frac{\partial}{\partial\theta}\left(F_{n,\kappa} e^{in\theta}\right) = \frac{in}{R_s} F_{n,\kappa} e^{in\theta} \tag{12}$$

which implies:

$$\left|\Lambda_{n,\kappa}\right| = \Lambda_{n,\kappa}^{\max} = \left|\frac{in}{R_s} F_{n,\kappa}\right| = \frac{n}{R_s} F_{n,\kappa}^{\max} \tag{13}$$

For the analytical model solution, the following simplifying assumptions are made: magnetic saturation in stator and rotor cores is neglected; the space between one magnet segment and the other is not considered; stator slotting effects are disregarded; permanent magnets are supposed to have uniform electrical conductivity σ and uniform magnetic permeability μ_0 (equal to the air permeability).

B. COMPUTATION OF MMF SPACE HARMONICS

To compute the MMF harmonics $F_{n,\kappa}^{\max}$, the three-phase winding design needs to be known. For this purpose, let us call Z the number of slots (in case of distributed winding) or wound teeth (in case of concentrated winding) and let us call A, B and C the stator phases. The slots (for distributed windings) or the teeth (for concentrated windings) are sequentially numbered from 1 to Z and identified by the integer index $u \in \{1, 2, \ldots, Z\}$. The phases, considering both goes and returns, are numbered as shown in Table 1 and identified by the integer index $v \in \{1, 2, \ldots, 6\}$.

Based on these conventions, the winding structure is univocally described by a $Z \times 6$ winding matrix $\mathbf{W}$ such that the element $[\mathbf{W}]_{\mathbf{u},\mathbf{v}}$ is equal to the number of turns of the phase v embedded in the u^{th} slot (for distributed windings) or wound around the u^{th} tooth (for concentrated windings).

As an example, let us consider the 9-teeth 8-poles winding arrangement shown in Figure 2.

The corresponding winding matrix is (14), where N_0 is the number of turns wound around each tooth.

$$\mathbf{W} = \begin{pmatrix} N_0 & 0 & 0 & 0 & 0 & 0 \\ 0 & 0 & 0 & N_0 & 0 & 0 \\ 0 & 0 & 0 & 0 & 0 & N_0 \\ 0 & 0 & N_0 & 0 & 0 & 0 \\ 0 & 0 & 0 & 0 & 0 & N_0 \\ 0 & N_0 & 0 & 0 & 0 & 0 \\ 0 & 0 & 0 & 0 & N_0 & 0 \\ 0 & N_0 & 0 & 0 & 0 & 0 \\ 0 & 0 & 0 & N_0 & 0 & 0 \end{pmatrix} \tag{14}$$

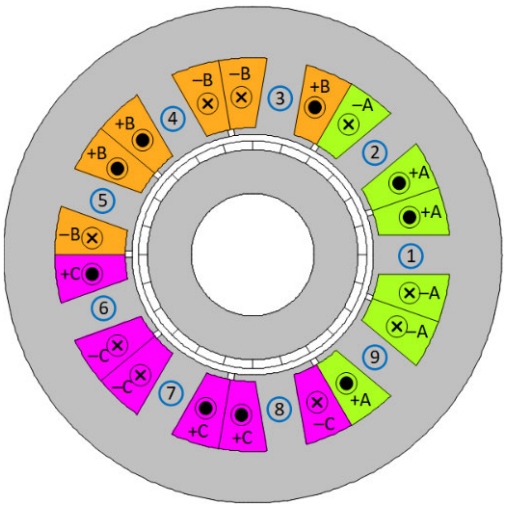

FIGURE 2. Phase arrangement for a 9-teeth 8-poles concentrated winding. Symbols ⊙ and ⊗ denote conventional current directions (respectively pointing outwards and inwards). A, B and C are the phases.

Once the winding matrix is defined, the magnitude of the MMF harmonics produced by the winding when energized with a symmetrical balanced set of currents of amplitude I_0 can be computed as explained in [32]. Specifically, the n^{th} order MMF space harmonic revolving in the same ($\kappa = +1$)

TABLE 1. Conventional numbering of stator phases.

Phase	Index
+ A	$v = 1$
– C	$v = 2$
+ B	$v = 3$
– A	$v = 4$
+ C	$v = 5$
– B	$v = 6$

or opposite ($\kappa = -1$) direction with respect to the rotor has an amplitude given by:

$$F_{n,\kappa}^{\max} = \left| \frac{a_n I_0}{2} \sum_{\substack{u=1,2,..,Z \\ v=1,2,..,6}} [\mathbf{W}]_{u,v} e^{i\left[-\frac{\pi}{3}(v-1)+\kappa n \frac{2\pi}{Z}(u-1)\right]} \right| \tag{15}$$

where

$$a_n = \frac{2}{\pi} \frac{(-1)^n}{n} \sin\left(\frac{\pi n(Z-1)}{Z}\right) \tag{16}$$

TABLE 2. Design details of the example machine.

Quantity	Value
Stator outer radius	113.5 mm
Stator bore radius, R_s	55 mm
Permanent magnet outer radius, R_m	52 mm
Rotor core outer radius, R_r	48 mm
Rotor core inner radius	28 mm
Mechanical air gap, R_s–R_m	3 mm
Permanent magnet height, R_m–R_r	4 mm
Magnetic gap, R_s–R_r	7 mm
Core length, L	100 mm
Stator back iron height	24 mm
Stator tooth width	18 mm
Stator slot opening width	2.8 mm
Stator slot opening height	3 mm
Number of poles, $2p$	8
Number of wound teeth, Z	9
Number of turns per tooth, N_0	25
Stator and rotor core relative permeability	10^4
Permanent magnet relative permeability	1
Permanent magnet electric conductivity, σ	0.667 MS/m
Stator current amplitude, I_0	100 A
Stator current angular frequency, ω_s	314 rad/s

For example, in the case of the machine taken as an example (Figure 2), the MMF space harmonics produced by the stator winding and computed through (14)- (16) are given in Figure 3 assuming a phase current amplitude $I_0 = 100$ A and a number of turns per tooth $N_0 = 25$. In the same plot, we have included the MMF space harmonics obtained from FE simulation of the same machine, whose design details are provided in Table 2. The MMF harmonics from FE analysis are obtained multiplying the magnetic field space harmonics by the magnetic air-gap width.

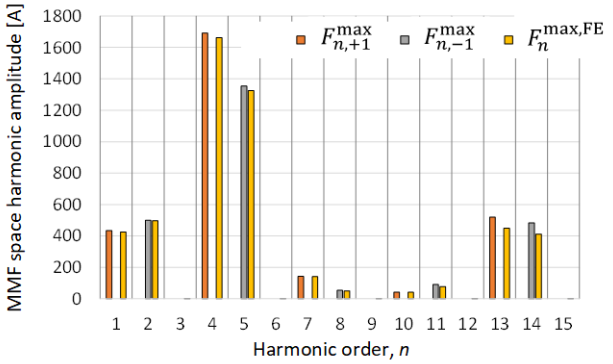

FIGURE 3. MMF harmonic amplitudes obtained analytically (orange bars if revolving in the rotor direction and grey bars if counter-rotating) and by FE analysis (yellow bars).

Limiting the attention to the first 15 space harmonics, Figure 3 shows that non-null harmonics rotating in the same direction as the rotor, obtained from (15) with $\kappa = +1$, have harmonic orders 1, 4, 7, 10 and 13, while non-null harmonics rotating opposite to the rotor, obtained from (15) with $\kappa = -1$, have orders 2, 5, 8, 11 and 14. Overall, the harmonic amplitudes computed through (15) are in good accordance with FE results.

III. ANALYTICAL MODEL SOLUTION

The magnetic and eddy-current field solutions for the space harmonic of order n revolving in the direction κ ($\kappa = 1$ meaning like the rotor and $\kappa = -1$ opposite to the rotor) can be expressed by solving partial-derivative differential equations involving the vector potential complex phasors $A_{n,\kappa}^{\text{air}}(r,\theta)$ and $A_{n,\kappa}^{\text{mag}}(r,\theta)$ respectively defined in the air gap and magnet regions. Specifically, in the air gap domain the vector potential $A_{n,\kappa}^{\text{air}}(r,\theta)$ satisfies the Laplace's equation:

$$\frac{1}{r}\frac{\partial}{\partial r}\left(r\frac{\partial A_{n,\kappa}^{\text{air}}}{\partial r}\right) + \frac{1}{r^2}\frac{\partial^2 A_{n,\kappa}^{\text{air}}}{\partial \theta^2} = 0 \tag{17}$$

while in the magnet region the vector potential $A_{n,\kappa}^{\text{mag}}(r,\theta)$ satisfies the Helmholtz's equation:

$$\frac{1}{r}\frac{\partial}{\partial r}\left(r\frac{\partial A_{n,\kappa}^{\text{mag}}}{\partial r}\right) + \frac{1}{r^2}\frac{\partial^2 A_{n,\kappa}^{\text{mag}}}{\partial \theta^2} + {k_{n,\kappa}}^2 A_{n,\kappa}^{\text{mag}} = 0 \tag{18}$$

where

$${k_{n,\kappa}}^2 = -i\omega_{n,\kappa}\sigma\mu_0 \tag{19}$$

Once the vector potential is known in the two regions, the magnetic flux density components in the air gap and magnets

can be derived as:

$$B_{n,\kappa}^{\mathrm{air},r} = \frac{1}{r}\frac{\partial A_{n,\kappa}^{\mathrm{air}}}{\partial \theta}, \quad B_{n,\kappa}^{\mathrm{air},\theta} = -\frac{\partial A_{n,\kappa}^{\mathrm{air}}}{\partial r} \tag{20}$$

$$B_{n,\kappa}^{\mathrm{mag},r} = \frac{1}{r}\frac{\partial A_{n,\kappa}^{\mathrm{mag}}}{\partial \theta}, \quad B_{n,\kappa}^{\mathrm{mag},\theta} = -\frac{\partial A_{n,\kappa}^{\mathrm{mag}}}{\partial r} \tag{21}$$

where $B_{n,\kappa}^{\mathrm{air},r}$ and $B_{n,\kappa}^{\mathrm{mag},r}$ denote the radial components while $B_{n,\kappa}^{\mathrm{air},\theta}$ and e $B_{n,\kappa}^{\mathrm{mag},\theta}$ denote the tangential components, respectively in the air gap and magnet region. It may be worth noting that the flux densities (20) and (21) have the meaning of spatial phasors, hence, for example, the actual flux density components in the air gap can be obtained as functions of both space and time from:

$$\mathcal{R}e\left(B_{n,\kappa}^{\mathrm{air},r}\left(r,\theta\right)e^{i\omega_{n,\kappa}t}\right),\ \mathcal{R}e\left(B_{n,\kappa}^{\mathrm{air},\theta}\left(r,\theta\right)e^{i\omega_{n,\kappa}t}\right) \tag{22}$$

The same applies to all the other complex phasors in the paper.

The solutions to (17) and (18) can be written in the form:

$$A_{n,\kappa}^{\mathrm{air}}\left(r,\theta\right) = e^{in\theta}\left(\hat{C}_{n,\kappa}r^{n} + \hat{D}_{n,\kappa}r^{-n}\right) \tag{23}$$

$$A_{n,\kappa}^{\mathrm{mag}}\left(r,\theta\right) = e^{in\theta}\left[\tilde{C}_{n,\kappa}J_{n}\left(k_{n,\kappa}r\right) + \tilde{D}_{n,\kappa}Y_{n}\left(k_{n,\kappa}r\right)\right] \tag{24}$$

where $\hat{C}_{n,\kappa}$, $\hat{D}_{n,\kappa}$,$\tilde{C}_{n,\kappa}$ and $\tilde{D}_{n,\kappa}$ are complex constants to be determined based on boundary conditions and $J_n\left(*\right)$ and $Y_n\left(*\right)$ represent Bessel functions of the first and second kind, respectively.

As regards the current density field in the magnet region, it has only the axial component and the relevant phasor $j(r,\theta)$ can be obtained from the vector potential as [33]:

$$\begin{aligned} j_{n,\kappa}\left(r,\theta\right) &= -i\omega_{n,\kappa}\sigma\left[A_{n,\kappa}^{\mathrm{mag}}\left(r,\theta\right) + \nabla_{z}\varphi_{n,\kappa}\left(r,\theta,z\right)\right] \\ &= -i\omega_{n,\kappa}\sigma A_{n,\kappa}^{\mathrm{mag}}\left(r,\theta\right) - i\omega_{n,\kappa}\sigma\nabla_{z}\varphi_{n,\kappa}\left(r,\theta,z\right) \end{aligned} \tag{25}$$

where ∇_z denotes the z component of the gradient operator and $\varphi_{n,\kappa}$ is an arbitrary continuously differentiable complex scalar function, which, for the sake of generality, is supposed to possibly depend on all the three cylindrical coordinates r, θ and z. Equation (25) descends from the fact that the vector potential is not uniquely defined and its possible values differ by the gradient of a function [33]. The function $\varphi_{n,\kappa}$ will be suitably set in the following so as to account for magnet segmentation.

A. MODEL SOLUTION WITHOUT SEGMENTATION

As a first step, we can find a solution assuming that all magnet segments are merged into a single annulus of uniform conductivity where the current is free to flow in the axial direction with no constraint [32]. Under this hypothesis, the solution can be plainly obtained by imposing the only boundary conditions:

$$B_{n,\kappa}^{\mathrm{air},\theta}\left(R_{\mathrm{s}},\theta\right) = -\left.\frac{\partial A_{n,\kappa}^{\mathrm{air}}}{\partial r}\right|_{r=R_{\mathrm{s}}} = \mu_{0}\Lambda_{n,\kappa}e^{in\theta} \tag{26}$$

$$\begin{aligned} B_{n,\kappa}^{\mathrm{air},\theta}\left(R_{m},\theta\right) &= -\left.\frac{\partial A_{n,\kappa}^{\mathrm{air}}}{\partial r}\right|_{r=R_{m}} \\ &= B_{n,\kappa}^{\mathrm{mag},\theta}\left(R_{m},\theta\right) = -\left.\frac{\partial A_{n,\kappa}^{\mathrm{mag}}}{\partial r}\right|_{r=R_{m}} \end{aligned} \tag{27}$$

$$\begin{aligned} B_{n,\kappa}^{\mathrm{air},r}\left(R_{m},\theta\right) &= \left.\frac{1}{r}\frac{\partial A_{n,\kappa}^{\mathrm{air}}}{\partial \theta}\right|_{r=R_{m}} \\ &= B_{n,\kappa}^{\mathrm{mag},r}\left(R_{m},\theta\right) = \left.\frac{1}{r}\frac{\partial A_{n,\kappa}^{\mathrm{mag}}}{\partial \theta}\right|_{r=R_{m}} \end{aligned} \tag{28}$$

$$B_{n,\kappa}^{\mathrm{mag},\theta}\left(R_{\mathrm{r}},\theta\right) = -\left.\frac{\partial A_{n,\kappa}^{\mathrm{mag}}}{\partial r}\right|_{r=R_{\mathrm{r}}} = 0 \tag{29}$$

Equation (26) prescribes that the tangential magnetic field on the stator bore surface must equal the current density at any point; equations (27)- (28) impose the continuity of the flux density across the magnet outer surface; equation (29) imposes the tangential flux density to vanish on the outer rotor core, supposed of infinite permeability.

Using the vector potential expressions (23)- (24) in (26)- (29) we obtain four linear equations in the unknows $\hat{C}_{n,\kappa}$, $\hat{D}_{n,\kappa}$,$\tilde{C}_{n,\kappa}$ and $\tilde{D}_{n,\kappa}$, which can be therefore easily determined. In particular we are interested in the two constants $\tilde{C}_{n,\kappa}$ and $\tilde{D}_{n,\kappa}$ which are involved in the current density expression in the magnet region (25).

From the boundary conditions (26)- (29) the following symbolic expressions are derived for $\tilde{C}_{n,\kappa}$ and $\tilde{D}_{n,\kappa}$:

$$\tilde{C}_{n,\kappa} = \Lambda_{n,\kappa}C_{n,\kappa} \tag{30}$$

$$\tilde{D}_{n,\kappa} = \Lambda_{n,\kappa}D_{n,\kappa} \tag{31}$$

with

$$C_{n,\kappa} = -2\mu_{0}{R_{\mathrm{m}}}^{n}{R_{\mathrm{s}}}^{n+1}Y_{n}^{'}\left(k_{n,\kappa}R_{\mathrm{r}}\right)/\Delta_{n,\kappa} \tag{32}$$

$$D_{n,\kappa} = 2\mu_{0}{R_{\mathrm{m}}}^{n}{R_{\mathrm{s}}}^{n+1}J_{n}^{'}\left(k_{n,\kappa}R_{\mathrm{r}}\right)/\Delta_{n,\kappa} \tag{33}$$

$$\begin{aligned} \Delta_{n,\kappa} = &\left[J_{n}^{'}\left(k_{n,\kappa}R_{\mathrm{m}}\right)Y_{n}^{'}\left(k_{n,\kappa}R_{\mathrm{r}}\right) - J_{n}^{'}\left(k_{n,\kappa}R_{\mathrm{r}}\right)Y_{n}^{'}\left(k_{n,\kappa}R_{\mathrm{m}}\right)\right] \\ &\times k_{n,\kappa}R_{\mathrm{m}}\left({R_{\mathrm{m}}}^{2n} + {R_{\mathrm{s}}}^{2n}\right) \\ &+\left[J_{n}^{'}\left(k_{n,\kappa}R_{\mathrm{r}}\right)Y_{n}\left(k_{n,\kappa}R_{\mathrm{m}}\right) - Y_{n}^{'}\left(k_{n,\kappa}R_{\mathrm{r}}\right)J_{n}\left(k_{n,\kappa}R_{\mathrm{m}}\right)\right] \\ &\times n\left({R_{\mathrm{m}}}^{2n} - {R_{\mathrm{s}}}^{2n}\right) \end{aligned} \tag{34}$$

In (32)- (34) we have introduced the derivatives of Bessel functions as follows [34]:

$$\begin{aligned} J_{n}^{'}(z) &= \frac{\partial J_{n}(z)}{\partial z} = \frac{J_{n-1}(z) - J_{n+1}(z)}{2}, \\ Y_{n}^{'}(z) &= \frac{\partial J_{n}(z)}{\partial z} = \frac{Y_{n-1}(z) - Y_{n+1}(z)}{2}. \end{aligned} \tag{35}$$

The expressions for $\hat{C}_{n,\kappa}$ and $\hat{D}_{n,\kappa}$ are omitted for the sake of brevity as they will not serve the purpose of eddy-current loss computation.

As regards the eddy-current field in the magnet region, in absence of segmentation we can choose $\varphi_{n,\kappa}\left(r,\theta,z\right) = 0$

in (25). So, based on (24), (25) and (30)- (31), we can write:

$$\begin{aligned} &j_{n,\kappa}^{\text{noseg}}(r,\theta) \\ &= -i\omega_{n,\kappa}\sigma A_{n,\kappa}^{\text{mag}}(r,\theta) \\ &= -i\omega_{n,\kappa}\sigma\,\Lambda_{n,\kappa}e^{in\theta}\left[C_{n,\kappa}J_n\left(k_{n,\kappa}r\right)+D_{n,\kappa}Y_n\left(k_{n,\kappa}r\right)\right] \end{aligned} \tag{36}$$

The choice $\varphi_{n,\kappa}(r,\theta,z) = 0$ is physically consistent because it assures the total current flowing through the magnet region (defined by $R_r < r < R_m$ and $0 < \theta < 2\pi$) to be zero. In fact:

$$\begin{aligned} &\int_{R_r}^{R_m}\int_0^{2\pi} j_{n,\kappa}^{\text{noseg}}(r,\theta)\,rd\theta dr \\ &= -i\omega_{n,\kappa}\sigma\,\Lambda_{n,\kappa}\int_{R_r}^{R_m}\left[\int_0^{2\pi}e^{in\theta}d\theta\right] \\ &\quad\times\left[C_{n,\kappa}J_n\left(k_{n,\kappa}r\right)+D_{n,\kappa}Y_n\left(k_{n,\kappa}r\right)\right]rdr = 0 \end{aligned} \tag{37}$$

because $\int_0^{2\pi} e^{in\theta}d\theta = 0$.

For the following it should be noted that $\left|j_{n,\kappa}^{\text{noseg}}(r,\theta)\right|^2$ does not depend on θ. In fact, from (36) and considering (9) we can write:

$$\begin{aligned} \left|j_{n,\kappa}^{\text{noseg}}(r,\theta)\right|^2 = \omega_{n,\kappa}{}^2\sigma^2\Lambda_{n,\kappa}^{\max 2}\left|C_{n,\kappa}J_n\left(k_{n,\kappa}r\right)\right. \\ \left.+D_{n,\kappa}Y_n\left(k_{n,\kappa}r\right)\right|^2. \end{aligned} \tag{38}$$

B. EDDY CURRENT DENSITY IN PRESENCE OF SEGMENTATION

In presence of segmentation, an additional constraint for the model solution beside (26)- (29) is that the currents cannot flow from one segment to the other. In other words, the net current through a segment should be zero. To satisfy the condition, we can define the current density within the m^{th} magnet segment according to (25) as follows:

$$j_{n,\kappa}^{\text{seg},m}(r,\theta) = -i\omega_{n,\kappa}\sigma A_{n,\kappa}^{\text{mag}}(r,\theta) - i\omega_{n,\kappa}\sigma\nabla_z\varphi_{n,\kappa}^m(r,\theta,z) \tag{39}$$

where we decide to define the scalar function $\varphi_{n,\kappa}^m$ as follows:

$$\varphi_{n,\kappa}^m(r,\theta,z) = z\,\frac{J_{n,\kappa}^m}{i\omega_{n,\kappa}\sigma} \tag{40}$$

In (40), $J_{n,\kappa}^m$ is a suitable constant to be determined. The z component of the gradient of $\varphi_{n,\kappa}^m(r,\theta,z)$ is:

$$\nabla_z\varphi_{n,\kappa}^m(r,\theta,z) = \frac{\partial\varphi_{n,\kappa}^m}{\partial z} = \frac{J_{n,\kappa}^m}{i\omega_{n,\kappa}\sigma} \tag{41}$$

Considering (36) and (41), we can thus express (39) as:

$$j_{n,\kappa}^{\text{seg},m}(r,\theta) = j_{n,\kappa}^{\text{noseg}}(r,\theta) - J_{n,\kappa}^m \tag{42}$$

The total current $I_{n,\kappa}^m$ flowing through the m^{th} segment, which spans over the cross-section region defined by (Figure 1)

$$R_r < r < R_m, \quad (m-1)\frac{2\pi}{M} < \theta < m\frac{2\pi}{M} \tag{43}$$

can be computed as:

$$I_{n,\kappa}^m = \int_{R_r}^{R_m}\int_{(m-1)\frac{2\pi}{M}}^{m\frac{2\pi}{M}} j_{n,\kappa}^{\text{seg},m}(r,\theta)\,rd\theta dr \tag{44}$$

which must be set equal to zero:

$$I_{n,\kappa}^m = 0 \tag{45}$$

This constraint enables us to define the constant $J_{n,\kappa}^m$ in (42) for the generic m^{th} magnet segment. In fact, from (42), (44) and (45) we have:

$$\begin{aligned} I_{n,\kappa}^m = &\int_{R_r}^{R_m}\int_{(m-1)\frac{2\pi}{M}}^{m\frac{2\pi}{M}} j_{n,\kappa}^{\text{noseg}}(r,\theta)\,rd\theta dr \\ &-\frac{\pi\left(R_m{}^2-R_r{}^2\right)}{M}J_{n,\kappa}^m = 0 \end{aligned} \tag{46}$$

which yields:

$$J_{n,\kappa}^m = \frac{M}{\pi\left(R_m{}^2-R_r{}^2\right)}\int_{R_r}^{R_m}\int_{(m-1)\frac{2\pi}{M}}^{m\frac{2\pi}{M}} j_{n,\kappa}^{\text{noseg}}(r,\theta)\,rd\theta dr \tag{47}$$

By using (36) for the expression of $j_{n,\kappa}^{\text{noseg}}(r,\theta)$, after symbolic integration with respect to the variable θ, we have:

$$\begin{aligned} J_{n,\kappa}^m = &\Lambda_{n,\kappa}\frac{M}{\pi\left(R_m{}^2-R_r{}^2\right)}\frac{\sigma\omega_{n,\kappa}}{n}e^{\frac{2\pi imn}{M}}\left(e^{-\frac{2\pi in}{M}}-1\right) \\ &\times\int_{R_r}^{R_m}\left(C_{n,\kappa}J_n\left(k_{n,\kappa}r\right)+D_{n,\kappa}Y_n\left(k_{n,\kappa}r\right)\right)rdr \end{aligned} \tag{48}$$

In particular, to obtain (48) we have used the following identity:

$$-i\int_{(m-1)\frac{2\pi}{M}}^{m\frac{2\pi}{M}} e^{in\theta}d\theta = \frac{1}{n}e^{\frac{2\pi imn}{M}}\left(e^{-\frac{2\pi in}{M}}-1\right) \tag{49}$$

Unfortunately, the integration with respect to the variable r cannot be performed symbolically in (48). Hence a closed-form expression for the integral in (48) cannot be given.

For the following of the paper it is worth noticing that $\left|J_{n,\kappa}^m\right|^2$ does not depend on m. In fact, from (48) and considering (9) we can write:

$$\begin{aligned} \left|J_{n,\kappa}^m\right|^2 = &4\left[\sin\left(\frac{\pi n}{M}\right)\right]^2\Lambda_{n,\kappa}^{\max 2}\frac{M^2}{\pi^2\left(R_m{}^2-R_r{}^2\right)^2}\frac{\sigma^2\omega_{n,\kappa}{}^2}{n^2} \\ &\times\left|\int_{R_r}^{R_m}\left(C_{n,\kappa}J_n\left(k_{n,\kappa}r\right)+D_{n,\kappa}Y_n\left(k_{n,\kappa}r\right)\right)rdr\right|^2 \end{aligned} \tag{50}$$

In particular, to obtain (50) from (48) we have used the following identity:

$$\left|e^{-\frac{2\pi in}{M}}-1\right|^2 = 4\left[\sin\left(\frac{\pi n}{M}\right)\right]^2 \tag{51}$$

C. PERMANENT MAGNET LOSS COMPUTATION

1) LOSSES WITHOUT SEGMENTATION

For the computation of the losses in permanent magnets, it is convenient to start with the model without segmentation. In this case, the eddy-current losses are:

$$P_{n,\kappa}^{\text{noseg}} = \frac{L}{2\sigma}\int_{R_r}^{R_m}\int_{0}^{2\pi}\left|j_{n,\kappa}^{\text{noseg}}(r,\theta)\right|^2 r d\theta dr \tag{52}$$

By using (38), after integration with respect to θ we find:

$$P_{n,\kappa}^{\text{noseg}} = \pi L\sigma {\omega_{n,\kappa}}^2 \Lambda_{n,\kappa}^{\max 2}\int_{R_r}^{R_m}\left|C_n J_n\left(k_{n,\kappa}r\right)+D_n Y_n\left(k_{n,\kappa}r\right)\right|^2 r dr \tag{53}$$

Unfortunately, the integral in (53) does now allow for symbolic solution and needs to be computed numerically.

2) LOSSES IN PRESENCE OF SEGMENTATION

As regards the model with segmentation, the total eddy current losses can be obviously found as:

$$P_{n,\kappa}^{\text{seg}} = \sum_{m=1}^{M} P_{n,\kappa}^{\text{seg},m} \tag{54}$$

where $P_{n,\kappa}^{\text{seg},m}$ are the losses that occur in the m^{th} magnet segment. The latter can be expressed as follows:

$$P_{n,\kappa}^{\text{seg},m} = \frac{L}{2\sigma}\int_{R_r}^{R_m}\int_{(m-1)\frac{2\pi}{M}}^{m\frac{2\pi}{M}}\left|j_{n,\kappa}^{\text{seg},m}(r,\theta)\right|^2 r d\theta dr \tag{55}$$

Through the detailed passages provided in Appendix A, the expression above can be equivalently written as follows:

$$P_{n,\kappa}^{\text{seg},m} = \frac{1}{M}P_{n,\kappa}^{\text{noseg}} - \frac{L}{2\sigma}\frac{\pi\left({R_m}^2-{R_r}^2\right)}{M}\left|J_{n,\kappa}^{m}\right|^2 \tag{56}$$

Since $\left|J_{n,\kappa}^{m}\right|^2$, given by (50), does not depend on m, summing all the loss contributions from the magnet segments according to (54) can be easily done as follows:

$$P_{n,\kappa}^{\text{seg}} = MP_{n,\kappa}^{\text{seg},m} = P_{n,\kappa}^{\text{noseg}} - \frac{L}{2\sigma}\pi\left({R_m}^2-{R_r}^2\right)\left|J_{n,\kappa}^{m}\right|^2 \tag{57}$$

As the last step, we can use the expressions (53) and (50) respectively for $P_{n,\kappa}^{\text{noseg}}$ and $\left|J_{n,\kappa}^{m}\right|^2$ in (54). The final formula for the total losses $P_{n,\kappa}^{\text{seg}}$ in presence of segmentation will be:

$$P_{n,\kappa}^{\text{seg},m} = \pi L\sigma {\omega_{n,\kappa}}^2 \Lambda_{n,\kappa}^{\max 2}\left[H_{n,\kappa} - K_{n,\kappa}\frac{\sin^2\left(\frac{\pi n}{M}\right)}{\left(\frac{\pi n}{M}\right)^2}\right] \tag{58}$$

where the two constants $H_{n,\kappa}$ and $K_{n,\kappa}$ are introduced for the sake of convenience and defined as follows:

$$H_{n,\kappa} = \int_{R_r}^{R_m}\left|C_{n,\kappa}J_n\left(k_{n,\kappa}r\right)+D_{n,\kappa}Y_n\left(k_{n,\kappa}r\right)\right|^2 r dr \tag{59}$$

$$K_{n,\kappa} = \frac{2\left|\int_{R_r}^{R_m}\left(C_{n,\kappa}J_n\left(k_{n,\kappa}r\right)+D_{n,\kappa}Y_n\left(k_{n,\kappa}r\right)\right)r dr\right|^2}{{R_m}^2-{R_r}^2} \tag{60}$$

Equivalently, the total losses can be expressed as a function of the MMF amplitude $\Lambda_{n,\kappa}^{\max}$ of the wave causing them. For this purpose, (13) can be used in (58) giving:

$$P_{n,\kappa}^{\text{seg},m} = \pi L\sigma {\omega_{n,\kappa}}^2 \frac{n^2 F_{n,\kappa}^{\max 2}}{{R_s}^2}\left[H_{n,\kappa} - K_{n,\kappa}\frac{\sin^2\left(\frac{\pi n}{M}\right)}{\left(\frac{\pi n}{M}\right)^2}\right] \tag{61}$$

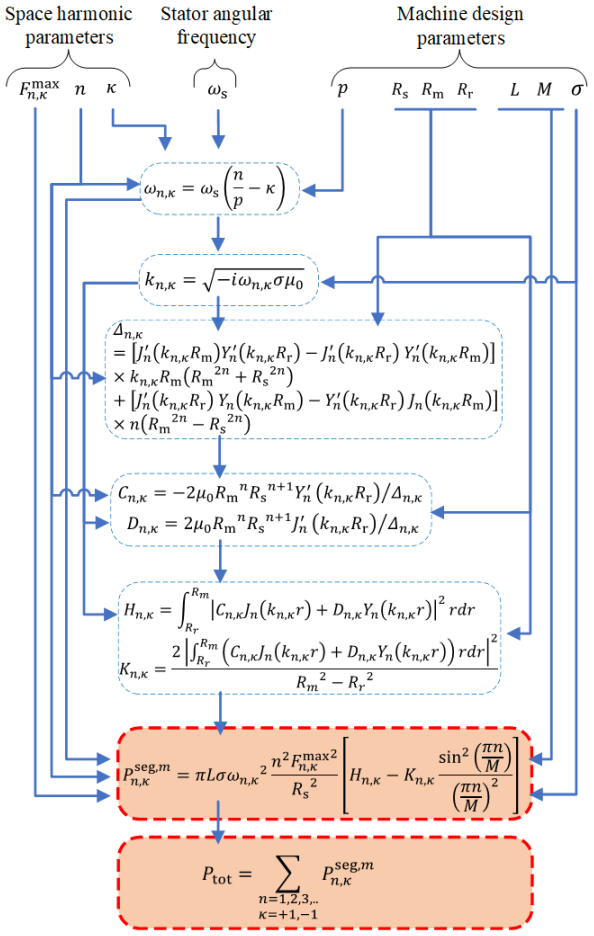

FIGURE 4. Flow chart summarizing the procedure for permanent magnet loss computation, from the input data to the final formula.

Finally, we can observe that the different space harmonics induce rotor eddy currents with different frequencies. Hence the superposition principle can be applied [35] leading to compute the total losses P_{tot} in the magnets as the sum of the losses caused by all the space harmonics:

$$P_{\text{tot}} = \sum_{\substack{n=1,2,3,..\\ \kappa=+1,-1}} P_{n,\kappa}^{\text{seg},m} \tag{62}$$

IV. PRACTICAL REMARKS ON MAGNET LOSS COMPUTATION

A. SYNOPSIS OF THE NUMERICAL PROCEDURE

Although the derivation of (58) or (61) is relatively lengthy, the computation of permanent magnet losses through (58)

or (61) is an easy numerical task which can be accomplished almost instantaneously in whatever engineering calculation environment.

For the sake of clarity and conciseness, the numerical procedure for permanent magnet loss computation in presence of radial segmentation of permanent magnets is summarized in Figure 4 as a flow chart.

In the flowchart, the calculation inputs are assumed to be the following:

- three parameters characterizing the air-gap magnetic wave which cause the losses: these are the MMF amplitude $F_{n,\kappa}^{\max}$ of the wave, its space harmonic order n and the parameter $\kappa = \pm 1$ used to identify the sense of rotation ($\kappa = 1$ for waves revolving in the same direction as the rotor, $\kappa = -1$ for counter-rotating waves);
- the stator angular frequency ω_s;
- the design parameters of the machine, i.e. the number of pole pairs p, the three radii R_s, R_m and R_r (Figure 1), the core length L, the number of permanent magnet segments M and the permanent magnet electrical conductivity σ.

All the passages involved in the algorithm are algebraic and in closed form except for:

- the evaluation of Bessel functions $J_n(*)$ and $Y_n(*)$ and their derivatives $J_n'(*)$ and $Y_n'(*)$ defined as per (35);
- numerical integration with respect to the variable r for the computation of the coefficients $H_{n,\kappa}$ and $K_{n,\kappa}$ according to (59) and (60).

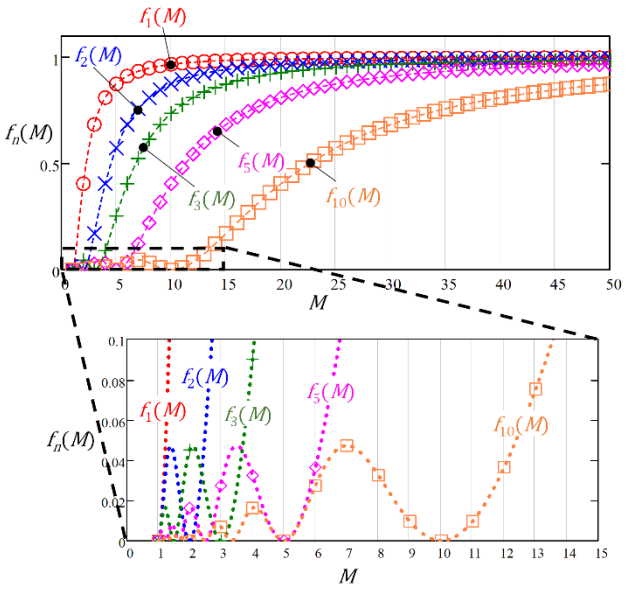

FIGURE 5. Diagrams of the function fn(M) for some values of the harmonic order n (n = 1, n = 2, n = 3, n = 5, n = 10) and zoomed view for 1<M<15.

Nevertheless, all mathematical engineering software tools include built-in efficient algorithms both for Bessel function evaluation and numerical integration.

B. DEPENDENCY OF THE LOSSES ON SEGMENTATION

From (58) or (61) it is clear that the number of magnet segments M appears only in these last formulas and, more precisely, in the non-negative function

$$f_n(M) = \frac{\sin^2\left(\frac{\pi n}{M}\right)}{\left(\frac{\pi n}{M}\right)^2} \tag{63}$$

which multiplies the coefficient $K_{n,\kappa}$. Looking at this function, we can notice that in case of no segmentation ($M = 1$) and for any space harmonic order n, we have:

$$P_{n,\kappa}^{\text{seg},m}\big|_{M=1} = \pi L \sigma {\omega_{n,\kappa}}^2 {\Lambda_{n,\kappa}^{\max}}^2 H_{n,\kappa} \tag{64}$$

because $\sin^2(\pi n) = 0$. Equation (64) in fact returns the losses given by (53) for the no-segmentation case.

Moreover, we can observe that, since both the function $f_n(M)$ and the coefficient $K_{n,\kappa}$ are non-negative according to (60) and (63), magnet segmentation always causes a beneficial reduction in the magnet losses, i.e. causes magnet losses to be strictly smaller than they would be in absence of segmentation. The only exception to this rule occurs when M is an integer divisor of the space harmonic order n. In this case the function $f_n(M)$ becomes zero because $\sin^2(\pi n/M) = 0$ and the losses in presence of segmentation become equal to the losses without segmentation. In other words, we can say that any space harmonic whose order n is an integer multiple of the number of magnet segments M causes the same losses that it would if there were no segmentation.

The diagrams of the function $f_n(M)$ is plotted in Figure 5 for different values of the space harmonic order n, specifically for $n = 1$, $n = 2$, $n = 3$, $n = 5$, $n = 10$. It is important to notice that, according to (58) or (61) and due to the coefficient $K_{n,\kappa}$ being non-negative, when the function $f_n(M)$ increases, the losses decrease and vice versa. It can be observed that for the space harmonic of order $n = 1$ (with one pole pairs), the function $f_n(M)$ is monotonic with respect to M. This means that the losses caused by the space harmonic wave of order $n = 1$ always decrease when the number of segments M increases.

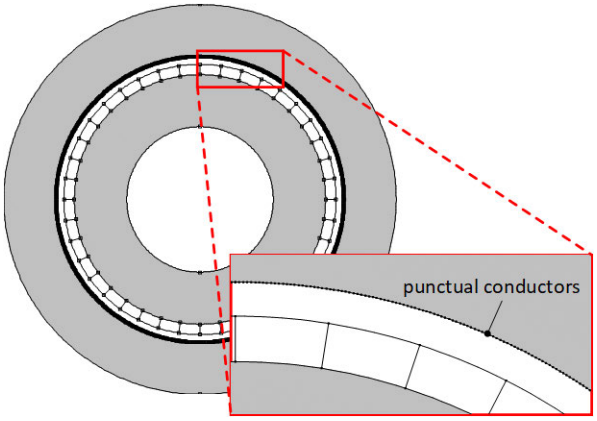

FIGURE 6. Model for FE validation of the permanent magnet losses due to a single space harmonic; zoomed view of a detail showing current points.

TABLE 3. Details of the FE model used for validation.

Quantity	Value
Stator bore radius, R_s	55 mm
Permanent magnet outer radius, R_m	52 mm
Rotor core radius, R_r	48 mm
Core length, L	100 mm
Permanent magnet conductivity, σ	0.667 MS/m
Permanent magnet relative permeability	1
Stator frequency, $\omega_s=\omega_{h,\kappa}$	314 rad/s
Linear current density amplitude, $\Lambda_{max} = \Lambda_{n,\kappa}^{max}$	2.026×10^5 A/m

For higher space harmonic orders, instead, the function is non-monotonic.

By studying the function $f_n(M)$ and its derivative as detailed in Appendix B, the following facts can be proved:

$$M < n \implies f_n(M) \leq 0.0472 \tag{65}$$

$$M > n \implies \frac{d}{dM} f_n(M) > 0 \tag{66}$$

$$\lim_{M\to\infty} f_n(M) = 1 \tag{67}$$

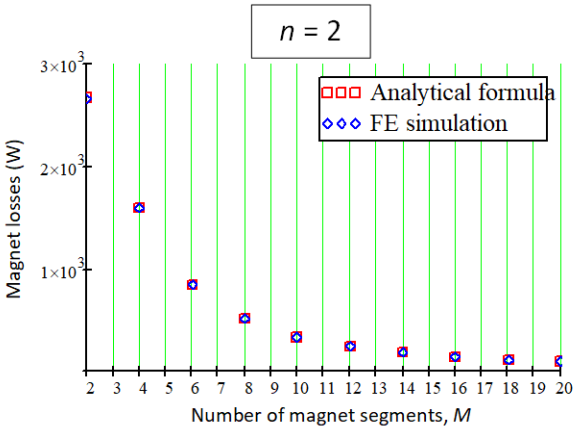

FIGURE 7. Permanent magnet losses from the analytical calculation and from FE analysis for space harmonic order n = 2.

The relationships listed above mean that, if the number of segments is less than the harmonic order, then the segmentation is very little effective in reducing the losses; instead, if the number of segments is larger than the harmonic order, the segmentation is beneficial and the losses monotonically decrease as the number of segments grows. The minimum losses that can be theoretically achieved, according to (67) applied to (58), is given below and would be achieved for the number of segments M tending to infinity:

$$\pi L \sigma \omega_{n,\kappa}{}^2 \Lambda_{n,\kappa}^{max2} \left[H_{n,\kappa} - K_{n,\kappa} \right], \tag{68}$$

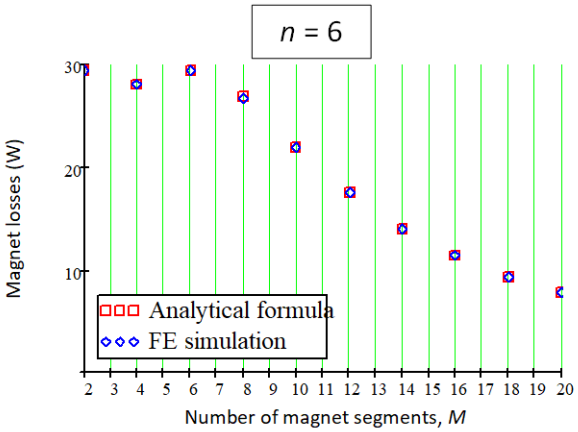

FIGURE 8. Permanent magnet losses from the analytical calculation and from FE analysis for space harmonic order n = 6.

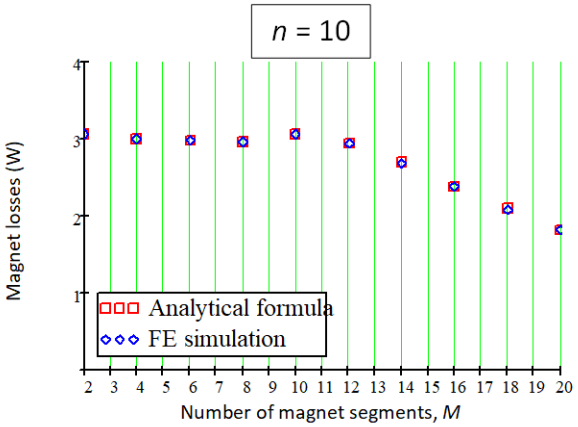

FIGURE 9. Permanent magnet losses from the analytical calculation and from FE analysis for space harmonic order n = 10.

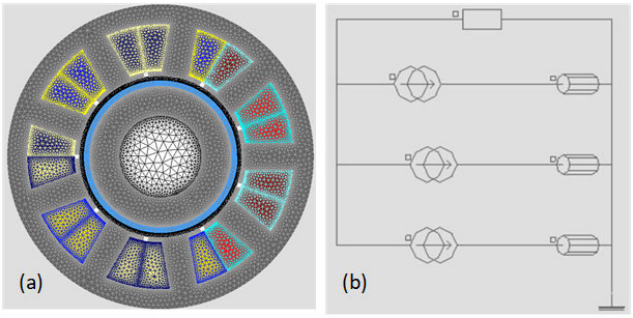

FIGURE 10. (a) Meshed model used for time-stepping FE analysis. (b) External circuit associated with the model to impress phase currents.

V. VALIDATION OF THE MAGNET LOSSES CAUSED BY A SINGLE SPACE HARMONIC

In this Section the formula (58) for magnet loss computation due to a single space harmonic is validated against FE simulations with the rotor at stand-still. The parameters treated

as variables in the simulations are the number of magnet segments M and the space harmonic order n.

To this end, the ideal model shown in Figure 1 is implemented in the form shown in Figure 6. The details of the model are provided in Table 3.

Since the rotor is at stand-still, the frequency of the induced eddy currents is equal to the stator frequency ω_s and the sense of direction of the MMF wave does not have any influence on the losses.

The effect of the single MMF space harmonic of order n is reproduced by a sinusoidal linear current density spread around the inner stator bore surface. Such current density is obtained by placing 1000 equally-spaced punctual conductors along the stator bore circumference (Figure 6). Numbering the punctual conductors sequentially from 1 to 1000, the following current complex phasor is assigned to the h^{th} punctual conductor:

$$\Lambda_{\max} \frac{2\pi R_s}{1000} e^{i\frac{2\pi n(h-1)}{1000}} \tag{69}$$

The resulting current distribution represents the discretization of a linear current density wave having amplitude $\Lambda_{\max}$ and n pole pairs and revolving at ω_s/n angular speed.

The FE analysis is run as a time-harmonic simulation at fixed angular frequency ω_s.

A comparison of the losses obtained with the proposed analytical approach and through FE analysis is shown in Figures 7, 8 and 9, which respectively refer to the harmonic orders $n = 2$, $n = 6$ and $n = 10$. The frequency of the stator currents (50 Hz) is maintained in all the three cases as well as the linear current density amplitude $\Lambda_{\max}$. For each harmonic order the number of magnet segments is varied in the range from 2 to 40 taking only even values.

It can be seen that the analytical results almost perfectly match FE simulation output in all cases.

Moreover, the results fully confirm that the segmentation is very little effective (or even detrimental) for $M < n$ while it always leads to loss reduction for $M > n$. Only under the latter condition, in fact, the losses decrease monotonically as the number of magnet segments grows.

VI. VALIDATION OF THE TOTAL LOSSES CAUSED BY THE STATOR WINDING

In this Section, the computation of eddy-current losses in the permanent magnets of a whole SPM machines will be considered. Its cross section is depicted in Figure 2 and its design data are provided in Table 2. The machine is supposed to operate at steady state and synchronous speed (750 r/min) with sinusoidal stator currents having amplitude $I_0 = 100$ A at 50 Hz frequency.

For the simulation, the machine is modelled in the Flux 2D environment and a transient analysis is run. The meshed model in depicted in Figure 10 along with the external circuit associated with it.

To test the robustness of the proposed computation algorithm, simulations are run for different numbers of magnet segments M, namely for $M = 1$ (ideal case of no segmentation), $M = 8$ (two segments per pole), $M = 16$ (four segments per pole), $M = 24$ (six segments per pole), $M = 32$ (eight segments per pole), $M = 40$ (ten segments per pole).

TABLE 4. Comparison of permanent magnet losses from FE analysis and from analytical computation.

Number of magnet segments, M	Losses from FE analysis (W)	Losses computed analytically (W)
1	205	210
8	112	120
16	43.6	50.8
24	23.1	28.1
32	14.3	17.8
40	9.74	12.2

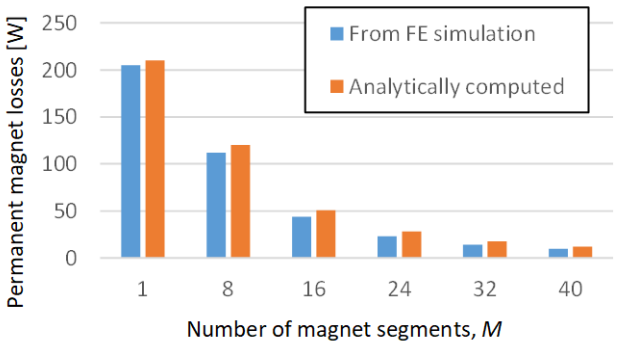

FIGURE 11. Comparison of permanent magnet losses computed from FE analysis and with the proposed analytical approach with different numbers of magnet segments.

For each number of segments, the total eddy-current losses in permanent magnets at steady state is extracted from the FE solutions.

The results are summarized in Table 4 along with the analytical predictions obtained from (62) following the flowchart given in Figure 4. The MMF space harmonics of orders $n = 1, 2, 3, \ldots, 30$ are considered and their amplitudes are computed from (14)- (16).

The results from FE simulation and analytical computation are also graphically provided in Figure 11.

Finally, the eddy-current loss computation is compared to FE results for different speeds of the machine and hence for different frequencies, taking the cases of 1, 3 and 5 magnet segments per pole (corresponding to a total number of segments equal to 8, 24 and 40, respectively). The results are provided in Figure 12.

Overall, we can observe a satisfactory matching between FE and analytical results. The discrepancies can be reasonably explained considering that the analytical procedure neglects slot openings, which cause a slight reduction in the MMF harmonic field amplitudes as it can be noticed in Figure 3. In fact, the losses predicted analytically appear to be slightly higher than those obtained from FE simulations for any number M of magnet segments.

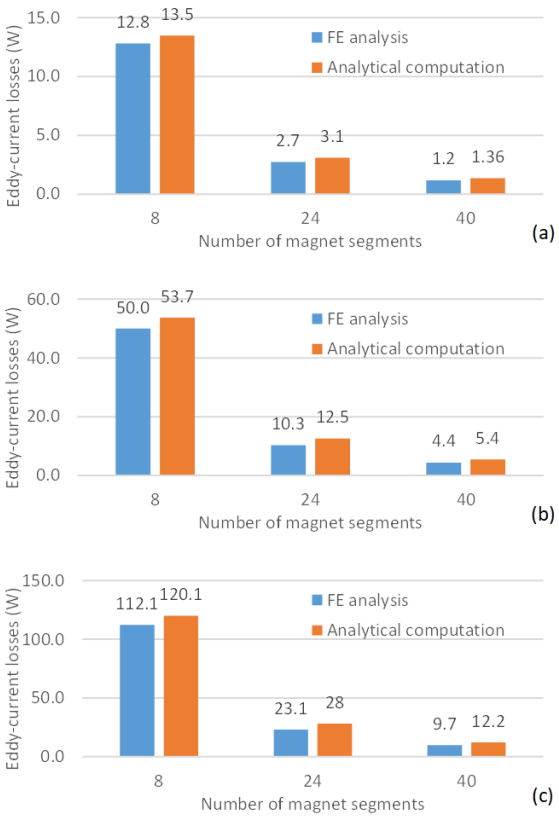

FIGURE 12. Eddy-current losses in permanent magnets computed by FE analysis and analytically for different number of magnet segments and different speeds: (a) 250 r/min; (b) 500 r/min; (c) 750 r/min.

VII. CONCLUSION

In this paper an accurate but simple algorithm has been presented for the fast computation of permanent magnet losses in a SPM machine in presence of circumferential segmentation. Compared to existing analytical methods, the proposed approach does not resort to Fourier series decomposition of field solutions and results in very easy-to-implement formulas. The axial segmentation is not explicitly addressed but can be accounted for through suitable correction coefficients proposed in existing literature. The final equations obtained can therefore be a valuable tool for the SPM machine designer to quickly and easily predict permanent magnet losses for different magnet segmentation options. The accuracy of the procedure has been extensively validated against FE analysis. In particular, the final expression obtained for permanent magnet losses indicates that the magnet segmentation is effective in reducing the losses caused by a given space harmonic of order n of the air-gap magnetic field only on condition that the number of segments exceeds the space harmonic order n.

Overall, the proposed algorithm is suitable for being incorporated in design optimization procedures aimed at reducing permanent magnet losses through the fast exploration of a wide variety of possible design solutions. It is reasonable that the best solutions thus identified are subsequently investigated more in depth, typically though FE analysis, to account for all design details and magnetic saturation effects.

Studies are presently in progress to obtain easy-to-use permanent-magnet loss computation algorithms incorporating 3D effects and thus directly applicable to magnet segmentation both in the axial and the circumferential direction.

APPENDIX A

In this Appendix, the analytical passages used to obtain (56) from (55) are provided in detail. In the passages, the complex conjugate of a complex number z will be indicated as $\bar{z}$.

Based on (42), equation (55) can be expanded as follows:

$$\begin{aligned} P_{n,\kappa}^{\text{seg},m} &= \frac{L}{2\sigma}\int_{R_r}^{R_m}\int_{(m-1)\frac{2\pi}{M}}^{m\frac{2\pi}{M}} \left|j_{n,\kappa}^{\text{seg},m}(r,\theta)\right|^2 r d\theta dr \\ &= \frac{L}{2\sigma}\int_{R_r}^{R_m}\int_{(m-1)\frac{2\pi}{M}}^{m\frac{2\pi}{M}} j_{n,\kappa}^{\text{seg},m}(r,\theta)\,\overline{j_{n,\kappa}^{\text{seg},m}(r,\theta)} r d\theta dr \\ &= \frac{L}{2\sigma}\int_{R_r}^{R_m}\int_{(m-1)\frac{2\pi}{M}}^{m\frac{2\pi}{M}} \left(j_{n,\kappa}^{\text{noseg}}(r,\theta) - J_{n,\kappa}^{m}\right) \\ &\quad \times \overline{\left(j_{n,\kappa}^{\text{noseg}}(r,\theta) - J_{n,\kappa}^{m}\right)} r d\theta dr = U_{n,\kappa}^{m} + V_{n,\kappa}^{m} + W_{n,\kappa}^{m}, \end{aligned} \tag{70}$$

where

$$U_{n,\kappa}^{m} = \frac{L}{2\sigma}\int_{R_r}^{R_m}\int_{(m-1)\frac{2\pi}{M}}^{m\frac{2\pi}{M}} \left|j_{n,\kappa}^{\text{noseg}}(r,\theta)\right|^2 r d\theta dr \tag{71}$$

$$V_{n,\kappa}^{m} = \frac{L}{2\sigma}\int_{R_r}^{R_m}\int_{(m-1)\frac{2\pi}{M}}^{m\frac{2\pi}{M}} \left|J_{n,\kappa}^{m}\right|^2 r d\theta dr \tag{72}$$

$$\begin{aligned} W_{n,\kappa}^{m} &= -\frac{L}{2\sigma}\int_{R_r}^{R_m}\int_{(m-1)\frac{2\pi}{M}}^{m\frac{2\pi}{M}} j_{n,\kappa}^{\text{noseg}}(r,\theta)\,\overline{J_{n,\kappa}^{m}} r d\theta dr \\ &\quad - \frac{L}{2\sigma}\int_{R_r}^{R_m}\int_{(m-1)\frac{2\pi}{M}}^{m\frac{2\pi}{M}\overline{j_{n,\kappa}^{\text{noseg}}}(r,\theta)} J_{n,\kappa}^{m} r d\theta dr \\ &= -\mathcal{R}e\left[\frac{L}{\sigma}\int_{R_r}^{R_m}\int_{(m-1)\frac{2\pi}{M}}^{m\frac{2\pi}{M}} j_{n,\kappa}^{\text{noseg}}(r,\theta)\,\overline{J_{n,\kappa}^{m}} r d\theta dr\right] \end{aligned} \tag{73}$$

In (73) we have considered that, for any complex number, z, the following property holds:

$$z + \bar{z} = 2\mathcal{R}e(z) \tag{74}$$

Regarding $U_{n,\kappa}^{m}$ in (71), we can remember that, according to (38), the integrand does not depend on θ. Hence, considering (52):

$$\begin{aligned} U_{n,\kappa}^{m} &= \frac{L}{2\sigma}\int_{R_r}^{R_m}\int_{(m-1)\frac{2\pi}{M}}^{m\frac{2\pi}{M}} \left|j_{n,\kappa}^{\text{noseg}}(r,\theta)\right|^2 r d\theta dr \\ &= \frac{1}{M}\left[\frac{L}{2\sigma}\int_{R_r}^{R_m}\int_{0}^{2\pi} \left|j_{n,\kappa}^{\text{noseg}}(r,\theta)\right|^2 r d\theta dr\right] = \frac{1}{M}P_{n,\kappa}^{\text{noseg}} \end{aligned} \tag{75}$$

Regarding $V_{n,\kappa}^{m}$ in (72), we can remember that $\left|J_{n,\kappa}^{m}\right|^2$ does not depend on m according to (50). Hence the integral in (72)

can be easily solved with respect to both r and θ, giving:

$$V_{n,\kappa}^{m} = \frac{L}{2\sigma}\frac{\pi\left(R_m{}^2 - R_r{}^2\right)}{M}\left|J_{n,\kappa}^{m}\right|^2 \tag{76}$$

Finally, let us consider (47) and multiply both sides of the equation by the complex constant $\overline{j_{n,k}^{m}}$. We obtain:

$$\begin{aligned} &J_{n,\kappa}^{m}\overline{J_{n,\kappa}^{m}} \\ &= \left|J_{n,\kappa}^{m}\right|^2 \\ &= \frac{M}{\pi\left(R_m{}^2 - R_r{}^2\right)}\int_{R_r}^{R_m}\int_{(m-1)\frac{2\pi}{M}}^{m\frac{2\pi}{M}} \overset{\text{noseg}}{J}_{n,\kappa}(r,\theta)\,\overline{J_{n,\kappa}^{m}}\,r d\theta dr \end{aligned} \tag{77}$$

which in turn gives:

$$\begin{aligned} &\int_{R_r}^{R_m}\int_{(m-1)\frac{2\pi}{M}}^{m\frac{2\pi}{M}} \overset{\text{noseg}}{J}_{n,\kappa}(r,\theta)\,\overline{J_{n,\kappa}^{m}}\,r d\theta dr \\ &= \frac{\pi\left(R_m{}^2 - R_r{}^2\right)}{M}\left|J_{n,\kappa}^{m}\right|^2. \end{aligned} \tag{78}$$

By substituting (78) into (73) we have:

$$W_{n,\kappa}^{m} = -\frac{L}{\sigma}\frac{\pi\left(R_m{}^2 - R_r{}^2\right)}{M}\left|J_{n,\kappa}^{m}\right|^2. \tag{79}$$

In conclusion, plugging (75), (76) and (79) into (70), the relationship (56) is obtained.

APPENDIX B

In this Appendix, the relationships (65)- (67) are formally proved.

The local maxima for $f_n(M)$ occur for values of M that are zeros of the first derivative of $f_n(M)$:

$$\begin{aligned} &\frac{d}{dM}f_n(M) \\ &= -\frac{2}{\pi^2 n^2}\sin\left(\frac{\pi n}{M}\right)\left[\pi n\cos\left(\frac{\pi n}{M}\right) - M\sin\left(\frac{\pi n}{M}\right)\right]. \end{aligned} \tag{80}$$

The derivative becomes zero when

$$\sin\left(\frac{\pi n}{M}\right) = 0 \tag{81}$$

and when

$$\pi n\cos\left(\frac{\pi n}{M}\right) - M\sin\left(\frac{\pi n}{M}\right) = 0 \tag{82}$$

Equation (82) can be equivalently written as:

$$\frac{\pi n}{M} = \tan\left(\frac{\pi n}{M}\right) \tag{83}$$

or as:

$$\frac{\sin^2\left(\frac{\pi n}{M}\right)}{\left(\frac{\pi n}{M}\right)^2} = f_n(M) = \cos^2\left(\frac{\pi n}{M}\right) \tag{84}$$

The condition (81) occurs when M is an integer divisor of n and leads to $f_n(M) = 0$, i.e. to local minima of $f_n(M)$. The local maxima of $f_n(M)$ therefore occur when the condition (83) and (84) are satisfied.

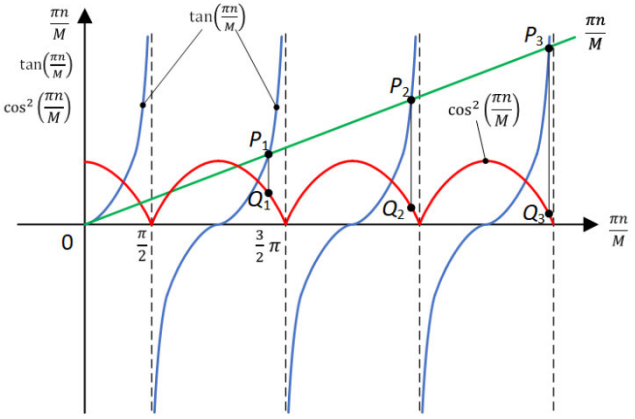

FIGURE 13. Function plots for the graphical determination of the local maxima for the function $f_n(M)$.

The solutions to (83), which cannot be found analytically, are the abscissas of the points P_1, P_2, P_3, ...in Figure 13. The corresponding values taken by the function $f_n(M)$ are, according to (84), the ordinates of the points $Q_1, Q_2, Q_3, \ldots$ It is apparent that the highest local maximum is the ordinate of point Q_1, whose coordinates are:

$$Q_1 \cong (4.493,\ 0.0472) \tag{85}$$

Therefore, we can state that the highest local maximum for the function $f_n(M)$ is 0.0472 and is taken for a number of magnet segments M such that:

$$\frac{\pi n}{M} \cong 4.493 \Longleftrightarrow M \cong 0.699 \times n \tag{86}$$

This is in total accordance with what can be observed in Figure 5 and proves (65) in a general manner.

As regards (66), it will be proven if we demonstrate that, for $M > n$, the following inequalities, involving the factors of the first derivative (80) of $f_n(M)$ with respect to M, hold:

$$\sin\left(\frac{\pi n}{M}\right) > 0 \tag{87}$$

$$\pi n\cos\left(\frac{\pi n}{M}\right) - M\sin\left(\frac{\pi n}{M}\right) < 0 \tag{88}$$

The former is certainly satisfied when $M > n$ because, in this case, the angle $\frac{\pi n}{M}$ falls in the range between 0 and π.

As to (88), it can be rewritten as:

$$\frac{\pi n}{M}\cos\left(\frac{\pi n}{M}\right) < \sin\left(\frac{\pi n}{M}\right) \tag{89}$$

If we study inequality (89) for $M > n$ then, again, the angle $\pi n/M$ falls in the range between 0 and π and, thus, two possible cases can occur.

When $\cos\left(\frac{\pi n}{M}\right) \leq 0$, i.e., $n < M \leq 2n$, this inequality it is certainly satisfied considering that $M\sin\left(\frac{\pi n}{M}\right)$ is positive for $M > n$.

If we instead suppose $\cos\left(\frac{\pi n}{M}\right) > 0$, which holds for $M > 2n$, we can rearrange (89) as:

$$\tan\left(\frac{\pi n}{M}\right) > \frac{\pi n}{M} \tag{90}$$

which is always satisfied for $\pi n/M < \pi/2$, as it can be seen in Figure 12.

In conclusion, we have proven that, when $M > n$, both inequalities (87) and (88) hold, which implies that the derivative (80) of $f_n(M)$ is positive under the same condition. This proves (66).

Finally, (67) is easily proven considering that:

$$\lim_{M\to\infty} f_n(M) = \lim_{\frac{\pi n}{M}\to 0} \left[\frac{\sin\left(\frac{\pi n}{M}\right)}{\frac{\pi n}{M}}\right]^2 = 1 \qquad (91)$$

REFERENCES

[1] K. Hu, G. Zhang, and W. Zhang, "Rotor design and optimization of high-speed surface-mounted permanent magnet motor based on the multi-physical field coupling method," *IEEE Access*, vol. 11, pp. 69614–69625, 2023.

[2] J. Ding, Z. Liu, Q. Chen, G. Liu, and G. Xu, "PM eddy current loss analysis and suppression in a spoke-type flux-modulation machine with magnetic flux barrier design," *IEEE Access*, vol. 11, pp. 125852–125860, 2023.

[3] F. Mahmouditabar, A. Vahedi, and F. Marignetti, "The demagnetization phenomenon in PM machines: Principles, modeling, and design considerations," *IEEE Access*, vol. 11, pp. 47750–47773, 2023.

[4] M. Baranski, W. Szelag, and W. Lyskawinski, "Experimental and simulation studies of partial demagnetization process of permanent magnets in electric motors," *IEEE Trans. Energy Convers.*, vol. 36, no. 4, pp. 3137–3145, Dec. 2021.

[5] P. Zhou, Y. Xu, and F. Xin, "Study of Magneto-thermal problems in low-speed high-torque direct drive PMSM based on demagnetization detection and loss optimization of permanent magnets," *IEEE Access*, vol. 11, pp. 92055–92069, 2023.

[6] D. Liang, Z. Q. Zhu, J. Feng, S. Guo, Y. Li, A. Zhao, and J. Hou, "Simplified 3-D hybrid analytical modelling of magnet temperature distribution for surface-mounted PMSM with segmented magnets," *IEEE Trans. Ind. Appl.*, vol. 58, no. 4, pp. 4474–4487, Jul. 2022.

[7] M.-M. Koo, J.-Y. Choi, K. Hong, and K. Lee, "Comparative analysis of eddy-current loss in permanent magnet synchronous machine considering PM shape and skew effect using 3-D FEA," *IEEE Trans. Magn.*, vol. 51, no. 11, Nov. 2015, Art. no. 6301104.

[8] B. Wex, S. Silber, K. Kaspar, and W. Gruber, "Fully automatized PWM loss calculation in multiphase PMSM and experimental verification," *IEEE Trans. Ind. Appl.*, vol. 58, no. 4, pp. 4237–4247, Jul. 2022.

[9] W.-Y. Huang, A. Bettayeb, R. Kaczmarek, and J.-C. Vannier, "Optimization of magnet segmentation for reduction of eddy-current losses in permanent magnet synchronous machine," *IEEE Trans. Energy Convers.*, vol. 25, no. 2, pp. 381–387, Jun. 2010.

[10] P. Zhang, G. Y. Sizov, J. He, D. M. Ionel, and N. A. O. Demerdash, "Calculation of magnet losses in concentrated-winding permanent-magnet synchronous machines using a computationally efficient finite-element method," *IEEE Trans. Ind. Appl.*, vol. 49, no. 6, pp. 2524–2532, Nov. 2013.

[11] S. S. Nair, L. Chen, J. Wang, R. Chin, I. Manolas, and D. Svechkarenko, "Computationally efficient 3D analytical magnet loss prediction in surface mounted permanent magnet machines," *IET Electr. Power Appl.*, vol. 11, no. 1, pp. 9–18, Jan. 2017.

[12] B. Aslan, E. Semail, and J. Legranger, "General analytical model of magnet average eddy-current volume losses for comparison of multiphase PM machines with concentrated winding," *IEEE Trans. Energy Convers.*, vol. 29, no. 1, pp. 72–83, Mar. 2014.

[13] L. Chen, J. Wang, and S. S. Nair, "An analytical method for predicting 3-D eddy current loss in permanent magnet machines based on generalized image theory," *IEEE Trans. Magn.*, vol. 52, no. 6, Jun. 2016, Art. no. 8103311.

[14] Z. Q. Zhu, K. Ng, N. Schofield, and D. Howe, "Analytical prediction of rotor eddy current loss in brushless machines equipped with surface-mounted permanent magnets. II. Accounting for eddy current reaction field," in *ICEMS. Proc. 5th Int. Conf. Electr. Mach. Syst.*, Shenyang, China, Aug. 2001, pp. 810–813.

[15] S. S. Nair, J. Wang, L. Chen, R. Chin, I. Manolas, and D. Svechkarenko, "Prediction of 3-D high-frequency eddy current loss in rotor magnets of SPM machines," *IEEE Trans. Magn.*, vol. 52, no. 9, Sep. 2016, Art. no. 8107910.

[16] M. Mirzaei, A. Binder, B. Funieru, and M. Susic, "Analytical calculations of induced eddy currents losses in the magnets of surface mounted PM machines with consideration of circumferential and axial segmentation effects," *IEEE Trans. Magn.*, vol. 48, no. 12, pp. 4831–4841, Dec. 2012.

[17] X. Wu, R. Wrobel, P. H. Mellor, and C. Zhang, "A computationally efficient PM power loss mapping for brushless AC PM machines with surface-mounted PM rotor construction," *IEEE Trans. Ind. Electron.*, vol. 62, no. 12, pp. 7391–7401, Dec. 2015.

[18] Z. Li, X. Huang, X. Xu, Z. Chen, Z. Jiang, L. Wu, T. Shi, and J. Zhang, "Nonlinear analytical model for predicting magnet loss in surface-mounted permanent-magnet motors," *IEEE Trans. Magn.*, vol. 58, no. 8, Aug. 2022, Art. no. 8203705.

[19] C. Bode and W.-R. Canders, "Advanced calculation of eddy current losses in PMSM with tooth windings," in *Proc. 19th Int. Conf. Electr. Mach.*, Rome, Italy, Sep. 2010, pp. 1–6.

[20] M. Mirzaei, "Eddy current analysis in permanent magnets using the variational method," *IEEE Trans. Magn.*, vol. 59, no. 10, pp. 1–11, Oct. 2023.

[21] F. Martin, M. E. Zaïm, A. Tounzi, and N. Bernard, "Improved analytical determination of eddy current losses in surface mounted permanent magnets of synchronous machine," *IEEE Trans. Magn.*, vol. 50, no. 6, Jun. 2014, Art. no. 8101209.

[22] S. Ruoho, T. Santa-Nokki, J. Kolehmainen, and A. Arkkio, "Modeling magnet length in 2-D finite-element analysis of electric machines," *IEEE Trans. Magn.*, vol. 45, no. 8, pp. 3114–3120, Aug. 2009.

[23] L. J. Wu, Z. Q. Zhu, D. Staton, M. Popescu, and D. Hawkins, "Analytical model of eddy current loss in windings of permanent-magnet machines accounting for load," *IEEE Trans. Magn.*, vol. 48, no. 7, pp. 2138–2151, Jul. 2012.

[24] S. S. Nair, J. Wang, R. Chin, L. Chen, and T. Sun, "Analytical prediction of 3-D magnet eddy current losses in surface mounted PM machines accounting slotting effect," *IEEE Trans. Energy Convers.*, vol. 32, no. 2, pp. 414–423, Jun. 2017.

[25] F. Dubas and A. Rahideh, "Two-dimensional analytical permanent-magnet eddy-current loss calculations in slotless PMSM equipped with surface-inset magnets," *IEEE Trans. Magn.*, vol. 50, no. 3, pp. 54–73, Mar. 2014.

[26] W. Tong, L. Sun, M. Hou, S. Wu, and R. Tang, "Analytical modeling for rotor eddy current loss of a surface-mounted PMSM with both non-ferromagnetic conductive retaining sleeve and shielding cylinder," *IEEE Trans. Energy Convers.*, vol. 37, no. 2, pp. 832–843, Jun. 2022.

[27] O. de la Barrière, S. Hlioui, H. B. Ahmed, and M. Gabsi, "An analytical model for the computation of no-load eddy-current losses in the rotor of a permanent magnet synchronous machine," *IEEE Trans. Magn.*, vol. 52, no. 6, Jun. 2016, Art. no. 8103813.

[28] B. Guo, Y. Huang, F. Peng, and J. Dong, "General analytical modeling for magnet demagnetization in surface mounted permanent magnet machines," *IEEE Trans. Ind. Electron.*, vol. 66, no. 8, pp. 5830–5838, Aug. 2019.

[29] F. Zhao, Z. Yu, J. Cao, and L. Li, "Design and optimization of a high-speed permanent magnet synchronous machine for gas compressors," *IEEE Trans. Magn.*, vol. 58, no. 2, Feb. 2022, Art. no. 8100905.

[30] M. Y. Metwly, M. S. Abdel-Majeed, A. S. Abdel-Khalik, R. A. Hamdy, M. S. Hamad, and S. Ahmed, "A review of integrated on-board EV battery chargers: Advanced topologies, recent developments and optimal selection of FSCW slot/pole combination," *IEEE Access*, vol. 8, pp. 85216–85242, 2020.

[31] F. Luise, S. Pieri, M. Mezzarobba, and A. Tessarolo, "Regenerative testing of a concentrated-winding permanent-magnet synchronous machine for offshore wind generation—Part I: Test concept and analysis," *IEEE Trans. Ind. Appl.*, vol. 48, no. 6, pp. 1779–1790, Nov. 2012.

[32] A. Tessarolo, "A quadratic-programming approach to the design optimization of fractional-slot concentrated windings for surface permanent-magnet machines," *IEEE Trans. Energy Convers.*, vol. 33, no. 1, pp. 442–452, Mar. 2018.

[33] G. B. Arfken, H. J. Weber, and F. E. Harris, *Mathematical Methods for Physicists: Vector Analysis*. New York, NY, USA: Academic, 2013, ch. 3, pp. 123–203.

[34] B. G. Korenev, *Bessel Functions and Their Applications*. Boca Raton, FL, USA: CRC Press, 2002.

[35] J. A. Svoboda and R. C. Dorf, *Introduction To Electric Circuits*. Hoboken, NJ, USA: Wiley, 2014, pp. 527–529.

CESARE CIRIANI received the Laurea degree in electrical engineering and the Ph.D. degree in industrial and information engineering from the University of Trieste, Trieste, Italy, in 2017 and 2023, respectively. He is currently the Scientific Laboratory Technician in charge of the Nondestructive Testing Laboratory "Domenico Di Santolo," University of Trieste. His research interests include electric machine analysis and design to nondestructive inspection of ropeway steel ropes with magneto-inductive equipment.

HAMID ALI KHAN received the B.S. and M.Sc. degrees in electrical engineering from COMSATS University Islamabad, Pakistan, in 2017 and 2020, respectively. He is currently pursuing the Ph.D. degree in industrial and information engineering with the University of Trieste, Italy. From 2019 to 2020, he was a Visiting Researcher with the College of Mechatronics and Control Engineering, Shenzhen University, Shenzhen, China. His research interests include design, analysis and optimization of high-speed electrical machines, permanent magnet synchronous machines, flux switching machines, and DC machines.

KIROLS MANSOUR received the B.S. degree in industrial engineering and the M.S. degree in electrical engineering from the University of Trieste, Italy, in 2018, and 2021, respectively, where he is currently pursuing the Ph.D. degree in industrial and information engineering. From 2020 to 2023, he was a Senior Electronics Engineer and the Quality Assurance Manager of the Research and Development Department, Illycaffè S.p.A., Trieste, Italy. His research interest includes the analysis and design of electric generation systems for renewable energy production.

MATTEO OLIVO received the M.Sc. degree in electrical engineering and the Ph.D. degree in industrial and information engineering from the University of Trieste, Trieste, Italy, in 2016 and 2020, respectively. From 2016 to 2019, he was with the Research and Development Department, Nidec ASI-Motors, Generators and Drives, Monfalcone, Italy. From 2020 to 2022, he was a Design Engineer with Danieli Automation, Buttrio, Italy. In 2022, he joined the Department of Engineering and Architecture, University of Trieste, where he is currently an Assistant Professor. His research interests include modeling, designing, and testing of rotating machines for industrial applications.

ALBERTO TESSAROLO (Senior Member, IEEE) received the Laurea degree in electrical engineering from the University of Trieste, Trieste, Italy, in 2000, and the Ph.D. degree in electrical engineering from the University of Padua, Padua, Italy, in 2011. He was involved in the design and development of large innovative motors, generators, and drives, from 2000 to 2006. Since 2006, he has been with the Engineering and Architecture Department, University of Trieste, where he is currently a Full Professor in charge of the courses of electric machine fundamentals and electric machine design. He has authored over 180 international articles in the areas of electrical machines and drives. He served as an Associate Editor for IEEE TRANSACTIONS ON INDUSTRY APPLICATIONS and *IET Electric Power Applications* from 2016 to 2021 and IEEE TRANSACTIONS ON ENERGY CONVERSION from 2013 to 2019. He was the Editor-in-Chief of IEEE TRANSACTIONS ON ENERGY CONVERSION from 2019 to 2022.

Open Access funding provided by 'Università degli Studi di Trieste' within the CRUI CARE Agreement